Eurasia Journal of Science and Technology
Print ISSN: 2663-1024
Online ISSN: 2663-1016
DOI: https://doi.org/10.61784/ejst3139

NON-DESTRUCTIVE TESTING METHOD FOR THE WIRE ROPE WITH DIFFERENT SURFACE WEAR

LiShuo Wu[1], Kun Huang[1*], GongNing Li[2,3], XiangDong Chang[1], LiQun Xiong[1], Zhou Zhou[2,3]
[1]*School of Mechanical and Electrical Engineering, National Key Laboratory of Intelligent Mining Equipment Technology, China University of Mining and Technology, Xuzhou 221116, Jiangsu, China.*
[2]*Key Laboratory of Intelligent Operation and Maintenance of High-Parameter Lifts, State Administration for Market Regulation, Suzhou 215031, Jiangsu, China.*
[3]*Jiangsu Special Equipment Safety Supervision and Inspection Institute, Jiangsu Province, Nanjing 210036, Jiangsu, China.*
[*]*Corresponding Author: Kun Huang*

Abstract: Steel wire ropes, as key load-bearing components, suffer from significant wear and broken wire damage during their service period, which poses a serious threat to operational safety. Addressing the issues such as the single excitation method in traditional eddy current detection methods, the large noise interference from the phase wave, and the low accuracy of damage quantitative identification, this paper proposes a new non-destructive testing method that combines a dual-level excitation structure with signal processing. Firstly, a dual-level excitation structure composed of three asymmetric magnetic poles on the left, middle, and right sides was designed. By using differentiated permanent magnet grades (N35/N52/N52) and a 60 mm magnetic pole spacing, two independent intervals with significantly different excitation intensities (up to 7.7%) were formed within the steel wire rope, effectively reducing mutual interference. Subsequently, through finite element simulation analysis, the influence of magnetic pole parameters on the excitation effect was investigated, and a signal processing method based on offset superposition and sliding average filtering was proposed to effectively suppress periodic phase wave noise. Experimental results show that this method established a high-precision cubic polynomial quantitative model between the number of broken wires and the peak-to-peak value of the eddy current signal (coefficient of determination $R^2 = 0.995$), and compared with existing detection devices, the error rate of broken wire identification was significantly reduced from 51.3% to 13.3%. This research provides an effective technical means for the precise quantitative identification of wire rope wear and broken wire damage, especially composite damage.
Keywords: Wire rope; Surface wear; Nondestructive testing

1 INTRODUCTION

As a key load-bearing component, wire rope is widely used in major engineering fields such as elevators, mines, and bridges. Its safe operation is directly related to the safety of life and property [1]. However, in the complex service environment, wire ropes are prone to local damage such as wire breakage and wear due to fatigue, wear and corrosion. These damages will significantly reduce their bearing capacity and even cause catastrophic accidents. Therefore, it is necessary to carry out regular and effective non-destructive testing of wire ropes to detect early damage in time. Among many non-destructive testing methods, the principle based on magnetic flux leakage testing has become the mainstream technology for wire rope testing because of its high sensitivity to ferromagnetic material defects and its applicability to on-site environments [2]. However, the traditional single excitation structure has significant limitations: on the one hand, the magnetic field generated by it is uniform, and it is difficult to effectively distinguish the periodic ' wave ' noise caused by the structure itself from the real damage signal. On the other hand, the single excitation intensity makes the response characteristics of different types or degrees of damage not rich enough, which limits the accuracy of quantitative identification. Therefore, it is necessary to develop a non-destructive testing device and method for wire rope with a new excitation structure to realize the detection of wire rope wear and broken wire damage, provide effective data support for quantitative identification of wire rope damage, and finally provide help for accurate prediction of wire rope lifespan.

The wear and fracture of the wire rope is one of the main reasons for the decline of its service performance. Cruzado et al. used laboratory fretting test and finite element simulation technology to explore the wear form and wear rate between steel wires under different loads and cross angles [3–5]. Wang solved the fretting fatigue parameters of steel wire rope under different terminal conditions by using dynamics, and explored the wear and crack propagation behavior of steel wire under different parameters [6–8]. Liu et al. studied the wear degradation of fatigue properties and structural strength of wire ropes by performing tensile fatigue and fracture tensile tests on wire ropes with different degrees of wear [9]. Chang et al. used a self-made test device to explore the sliding wear behavior of wire rope under different service conditions [10-11], and analyzed its wear mechanism and residual strength. Wang et al. explored the fretting fatigue wear behavior of wire rope in corrosive environment [12], and found that the synergistic effect of corrosion and fatigue would aggravate the wear of steel wire.

In the field of wire rope damage detection, in order to overcome the inherent limitations of traditional electromagnetic excitation methods in sensitivity, spatial resolution and working condition adaptability, scholars have carried out systematic and in-depth research on excitation mode optimization, sensor innovation and multi-physical field information fusion. In order to analyze the quantitative detection of broken wire of wire rope, Mzurek et al. carried out the research on the detection of wire rope by using geomagnetic field [13], and analyzed the influence of sensor arrangement on the defect detection results. Zhang et al. proposed a new method for quantitative detection of internal and surface defects of wire ropes by improving the shortcomings of induction coil magnetic flux detection and Hall sensor magnetic flux leakage detection [14]. Yan et al. proposed a simple magnetic flux leakage detection circuit based on the magnetic field measured by a single Hall sensor and two methods of using the iron core as the skeleton of the detection coil group to enhance the strength of the magnetic flux leakage signal when the wire rope is defective [15-16]. Based on Hall sensor and magnetic flux leakage detection method, Liu et al. carried out experimental research on local broken wire defects of wire rope [17], designed a detection device, and compared and analyzed the influence of different filtering methods on the detection results. Zhang et al. designed a small detector with simple structure [18], convenient installation, light weight and good portability, and used the instantaneous phase solution and wavelet analysis in Hibert transform to eliminate the interference waveform. In order to improve the recognition rate of magnetic flux leakage detection, Zhang et al. fused the magnetic image converted by the magnetic flux leakage information on the surface of the wire rope with the visible image of the wire rope [19], and achieved good results. At the same time, Zhang et al. proposed a method to further improve the recognition rate of wire rope defects by extracting the color moment and texture features of the pseudo-color magnetic flux leakage defect image of the wire rope and its color infrared defect image [20-21]. Liu et al. found that the algorithm based on the reshaped sine function transform is the most suitable for quantitative modeling of steel wire rope and defect signal recognition by comparing a variety of magnetic flux leakage imaging algorithms [22]. Gabor filtering, morphological filtering and small target extraction are used for magnetic flux leakage image processing and feature extraction, and a new type of magnetic flux leakage imaging and defect quantitative recognition method is proposed. In addition, Cao et al. studied the application of eddy current testing technology in non-destructive testing of wire ropes [23], proposed a wire rope broken wire identification method based on radial basis function neural network, and developed an experimental eddy current sensor and a computer measurement system. Aiming at the problem of weak signal in non-destructive testing of steel wire rope defects by magnetic flux leakage detection method in electromagnetic interference environment. Based on the magnetic flux leakage method, Peng et al. proposed a method for identifying the damage width of multi-channel fusion wire rope of Hall sensor array [24], which improved the detection accuracy of wire rope damage width. Pawel et al. systematically studied the resolution of 'passive magnetic method' in nondestructive testing of wire rope [25]. It is found that this method can find the surface defects of the wire rope, but when the defects are too close, the signals will interfere with each other and it is difficult to distinguish. Lu et al. combined magnetic flux leakage detection and infrared thermal imaging methods to improve the accuracy of wire rope broken wire damage identification based on fusion features [26].

Due to the limitations of traditional electromagnetic excitation methods, many scholars have turned their attention to alternative physical fields, and systematically carried out research on non-destructive testing of steel wire ropes based on multi-field coupling of heat, sound, and light. Feng et al. developed a set of 'portable energization-infrared imaging 'automatic detection system for measuring the corrosion rate of galvanized steel wire [27]. By heating the old steel wire and collecting the surface temperature rise, a cubic polynomial model of ' corrosion rate temperature rise ' was established. It was found that the higher the temperature, the heavier the corrosion. In order to further improve the accuracy of wire rope damage detection, according to the corrosion damage characteristics of wire rope, Neslušan et al. analyzed the relationship between Barkhausen noise parameters and corrosion depth of wire rope, and studied the non-destructive detection method of wire rope corrosion state by using Barkhausen noise [28]. Aiming at the problem that the actual service environment of wire rope is harsh, the noise is large, and the defect data is many and complex, Zhang et al. proposed a new flaw detection method based on convolutional denoising autoencoder and isolation forest [29], and verified its effect. Larson et al. used CCD camera to realize the recognition and detection of steel wire surface scratches [30]. Zhou et al. proposed a new method of wire rope damage detection based on texture features by extracting features from the surface image of wire rope [31]. Chen et al. designed a wire rope broken wire damage detection system based on magnetic leakage and visible light [32]. Through MEEMD-wavelet denoising, guided image filtering fusion magnetic signal, WTCAE positioning visible light defect and quantitative recognition of fusion image, the sensitivity and accuracy of broken wire recognition and positioning are significantly improved. Artificial intelligence has become the underlying engine that enables various technologies. Whether it is processing visual images, magnetic signals, or fusion features, deep learning has significantly improved the level of automation and intelligence of detection. Huang et al. constructed an automatic identification framework for surface damage of steel wire ropes based on convolutional neural networks (CNN) [33]. The study verified the effectiveness of deep visual features in detecting surface defects of steel wire ropes, but it was only applicable to visible surface damages in the laboratory and could not detect internal defects. Zhou et al. established a steel wire rope damage detection framework based on deep learning [34]. This framework significantly improved the intelligence and accuracy of damage detection through image preprocessing and deep convolutional neural networks.

Therefore, this paper proposes an innovative two-stage excitation structure and asymmetric magnetic pole design. This structure adopts different grades of permanent magnets for specific arrangement, aiming to actively construct two independent intervals with significantly different excitation intensities on the steel wire rope, thereby generating two different intensity leakage magnetic field signals due to the same damage. Based on this, corresponding signal

processing algorithms were developed, which effectively suppress the sheave wave noise through signal superposition and filtering. Finally, through the finite element simulation of the system, experimental calibration, and comparative tests with existing equipment, the proposed method was verified to improve the wear and broken wire damage of the steel wire rope

2 WIRE ROPE EXCITATION STRUCTURE AND EXCITATION SIMULATION ANALYSIS

2.1 Two-Stage Excitation Structure Design

The material of wire rope is carbon steel with high permeability. The material of wire rope is carbon steel with high permeability. In this paper, an innovative design of two-stage excitation structure is adopted, which is composed of Nd-Fe-B magnets and magnetic boots arranged by left, middle and right magnetic poles according to certain rules. Among them, two independent excitation intervals are formed between the three groups of permanent magnets and the magnetic boots, and different grades of magnets are used. The two-stage excitation structure includes a magnetic shoe (soft magnetic material) and a NdFeB magnet, as shown in Figure 1. At the same time, in order to prevent the permanent magnet from rotating along the central axis due to the repulsion of the magnetic poles, a stopper is added at both ends of the permanent magnet, which is fixed to the magnetic boot through bolts.

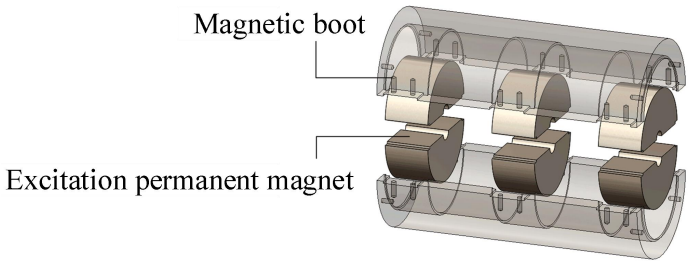

Figure 1 Dual-Stage Excitation Structure Diagram

In order to realize the convenient opening and closing of the device to load and unload the wire rope, the excitation structure adopts a double excitation circuit, as shown in Figure 2. The six NdFeB magnets are semi-annular, group 1 and group 3 are radially magnetized, and group 2 is axially magnetized. Among them, the bipolar polarity of group 1 is internal N and external S, the bipolar polarity of group 2 is left S and right N, and the bipolar polarity of group 3 is internal S and external N. The permanent magnet group 1, 3, magnetic boots and the measured wire rope form an overall magnetic induction line loop. Because of the axial magnetization of the permanent magnet group 2, the whole loop is divided into two independent intervals. In this magnetic circuit, there is an air gap Δ between the wire rope and the excitation structure, and the air gap Δ determines the size of the reluctance in the main magnetic circuit, so the air gap Δ should be reduced. This chapter mainly focuses on the design of 6 × 19 + FC wire rope (diameter 10 mm) to ensure that the air gap range is 1-2 mm and reduce the influence of air gap on the excitation effect.

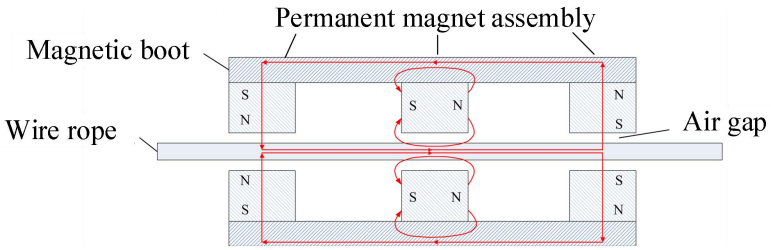

Figure 2 Schematic Diagram of Magnetic Poles and Magnetic Field Lines in a Two-Stage Excitation Structure

2.2 Finite Element Simulation of the Excitation Effect of the Two-Stage Excitation Structure

According to the new two-stage excitation structure model, a simplified ANSYS Maxwell finite element model is established. The simplified two-stage excitation structure is shown in Figure 3.

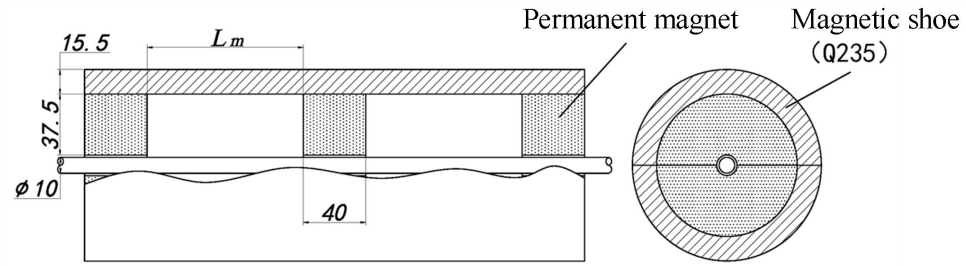

Figure 3 Simplified Finite Element Simulation Model of the Two-Stage Excitation Structure

The simulation analysis is based on a fixed magnetic pole spacing of 60 mm, and the permanent magnet group 1 is set to three different grades (N35, N40, N52) NdFeB permanent magnets, and the excitation intensity distribution cloud diagram of the wire rope is obtained as shown in Figure 4. It can be found that there is a part of the area where the magnetic induction intensity decreases below the permanent magnet group 2. The area is due to the cancellation of the magnetic induction lines, so that the part of the steel wire rope in the group 2 is demagnetized to a certain extent and re-excited in the next interval to reduce the excitation effect of the previous interval.

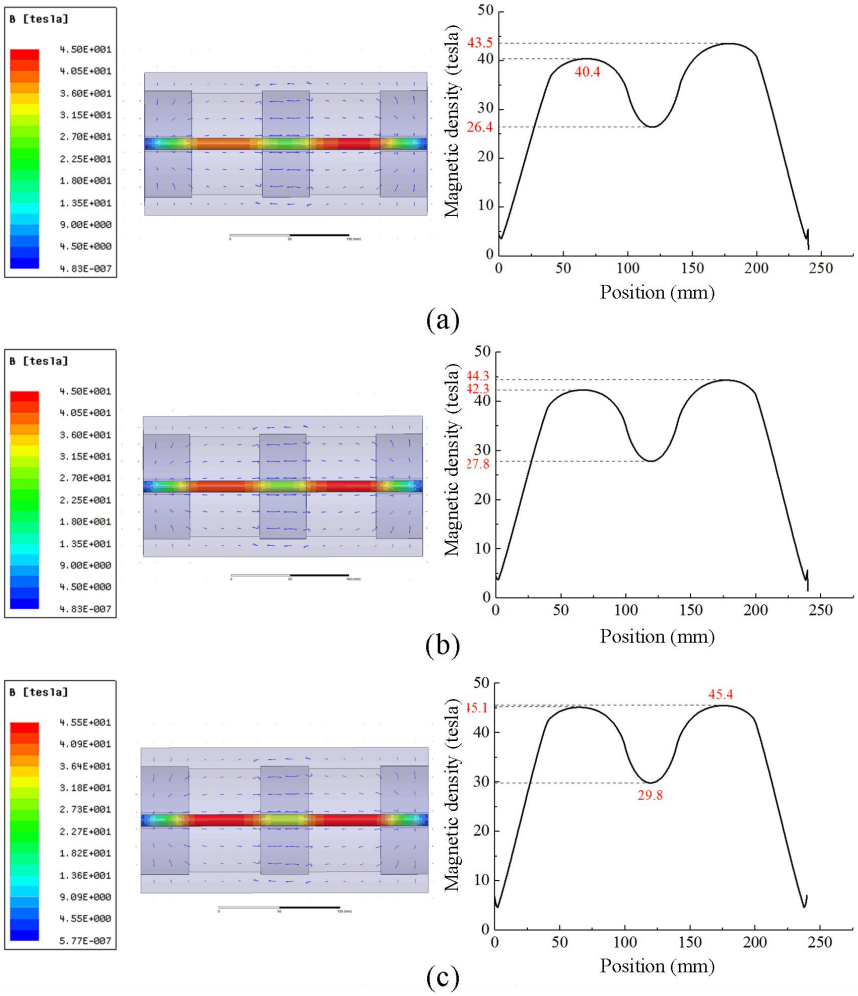

Figure 4 Cloud Charts of Magnetic Field Distribution Produced by Different Grades of Permanent Magnets and Curves of Magnetic Induction Intensity Variation of Steel Wire Ropes: (a) N35, (b) N40, (c) N50

Table 1 shows the relationship between the permanent magnet grade and the excitation intensity. It can be found that when the permanent magnet group 1 adopts the N50 grade Nd-Fe-B magnet, the excitation intensity between the permanent magnet group 1 and 2 is the strongest, followed by the N40 grade Nd-Fe-B magnet, and the N35 grade Nd-Fe-B permanent magnet, the excitation intensity between the permanent magnet group 1 and 2 is the weakest. It can be seen from the curve of the magnetic density of the steel wire rope that when the permanent magnet group 1 adopts the N35 grade NdFeB magnet, the peak value of the left excitation area is 40.4 T, the peak value of the right side is 43.5 T, and the intensity difference is 7.7 %. When the permanent magnet group 1 used the N40 grade NdFeB magnet, the left peak was 42.3 T, the right peak was 44.3 T, and the intensity difference was 4.7 %. When the permanent magnet group 1 used the N50 grade NdFeB magnet, the left peak was 45.1 T, the right peak was 45.4 T, and the intensity difference

was 0.7 %. At the same time, when the permanent magnet group 1 adopts the N35 brand permanent magnet, the demagnetization intensity ratio is 34.7 %, when the N40 permanent magnet is used, the demagnetization intensity ratio is 34.3 % ; when using N50 permanent magnet, the demagnetization intensity ratio is 33.9 %.

Table 1 Correspondence between Permanent Magnet Types and Excitation Strength

Brand name	Left-side excitation intensity (T)	Right-side excitation intensity (T)	Demagnetization intensity (T)	Excitation intensity difference	Difference in demagnetization intensity
N35	40.4	43.5	26.4	7.7%	34.7%
N40	42.3	44.3	27.8	4.7%	34.3%
N52	45.1	45.4	29.8	0.7%	33.9%

In summary, when the permanent magnet group 1 adopts the N35 grade Nd-Fe-B permanent magnet the permanent magnet group 2 and 3 adopt the N52 grade Nd-Fe-B permanent magnet), the maximum difference in the excitation intensity between the left and right excitation intervals is 7.7 %. Therefore, using this permanent magnet grade distribution scheme, a relatively large difference in excitation intensity can be obtained, and then two kinds of damage leakage magnetic fields with obvious intensity differences can be formed, thus providing a basis for subsequent leakage magnetic field detection and two intensity signal identification analysis. Under this condition, the demagnetization effect of permanent magnet group 2 is more obvious than that of the other two cases, which makes the interval with strong excitation ability on the right side have less influence on the left interval, and avoids the mutual interference between the two excitation intervals to a certain extent, so that the excitation results are more reliable. Therefore, three sets of permanent magnets are used in the two-stage excitation structure: permanent magnet group 1 (N35), permanent magnet group 2 (N52), and permanent magnet group 3 (N52).

In addition, the magnetic pole spacing is set to 60 mm, 80 mm and 100 mm respectively, and the magnetic field distribution cloud diagram and the magnetic density change curve inside the wire rope are obtained, as shown in Figure 5 Moreover, the corresponding relationship between the magnetic pole spacing and the excitation intensity is obtained, as shown in Table 2.

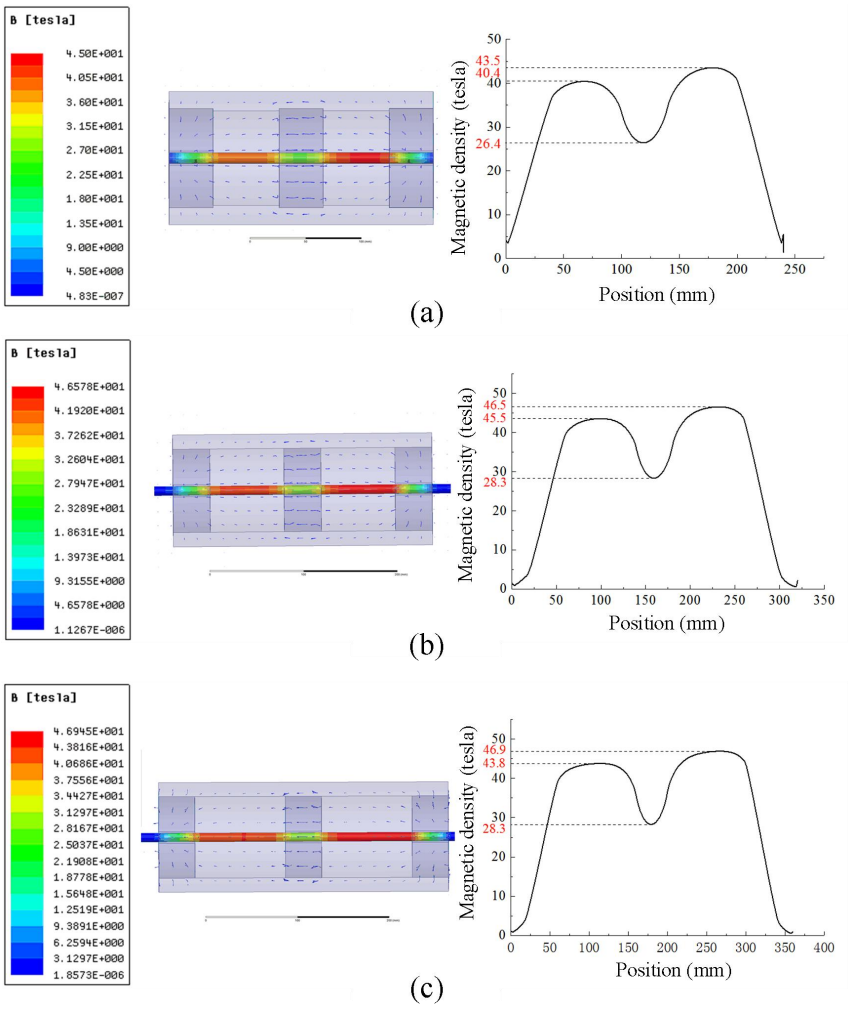

Figure 5 Magnetic Field Distribution Diagrams and Steel Wire Rope Magnetic Induction Intensity Change curves Resulting from Different Magnetic Pole Spacings: (a) 60 mm, (b) 80 mm, (c) 100 mm

Table 2 Relationship between Magnetic Pole Distance and Excitation Intensity

Magnetic pole gap (mm)	Left-side excitation intensity (T)	Right-side excitation intensity (T)	Demagnetization intensity (T)	Excitation intensity difference	Difference in demagnetization intensity
60	40.4	43.5	26.4	7.7%	34.7%
80	45.5	46.5	28.3	2.2%	37.8%
100	43.8	46.9	28.3	7.1%	35.4%

In the three groups of simulation results, the excitation intensity of the wire rope section in the excitation structure is supersaturated, and there are two excitation intervals between the permanent magnet group 1,2 and the permanent magnet group 2,3, and the excitation intensity is different. In the two excitation intervals, there is an obvious demagnetization area, indicating that the magnetic pole spacing does not essentially affect the magnetic field distribution. Through the magnetic density cloud diagram, it can be seen that with the increase of the magnetic pole spacing, the magnetic induction intensity of the wire rope increases first and then decreases. When the magnetic pole spacing is 60 mm, the maximum difference of excitation intensity is 7.7 %. When the magnetic pole spacing is 80 mm, although the wire ropes on both sides of the excitation interval produce higher excitation intensity, the excitation intensity difference is only 2.2 %, which is much smaller than the intensity difference of 7.7 % when the magnetic pole spacing is 60 mm, and also smaller than the intensity difference of 7.1 % when the magnetic pole spacing is 100 mm. Therefore, the magnetic pole spacing of 60 mm has better excitation intensity difference. In addition, the proportion of demagnetization intensity under the three magnetic pole spacings is 34.7 %, 37.8 % and 35.4 %, respectively, showing a trend of increasing first and then decreasing with the increase of spacing. Since the demagnetization intensity ratio is a secondary factor in the measurement of excitation effect, although the demagnetization intensity ratio is greater than the demagnetization intensity ratio when the magnetic pole spacing is 80 mm and 100 mm, the excitation intensity difference is given priority. Considering the influence of structural size and increasing spacing on the volume and mass of the whole device, the 60 mm magnetic pole spacing is selected as the design parameter of the device.

Based on the above results, two fracture defects with a spacing of 1 mm and a depth of 0.6 mm, 1 mm and 1.6 mm were set on the surface of the steel wire rope to simulate the concentrated wire breakage damage of the steel wire with a surface diameter of 0.6 mm, 1 mm and 1.6 mm, respectively. The damage model is imported into the simulation software to obtain the magnetic induction intensity cloud diagram and the magnetic field intensity change curve of the wire rope surface, as shown in Figure 6. The two-stage excitation structure generates two excitation intervals with different magnetic induction intensity on the wire rope, and on this basis, a certain intensity of leakage magnetic field is generated at the fracture. It can be seen from the figure that the darker the color in the magnetic induction intensity cloud diagram indicates the stronger the magnetic induction intensity at this place. The cloud image at the right fracture in the above cloud diagram is obviously darker, indicating that the right fracture corresponding to different fracture depths has different leakage magnetic fields than the left fracture. The specific amplitude of the leakage magnetic field can be seen from the curve changes in the figure. The numerical results are shown in Table 3. It can be seen from the change of leakage magnetic field amplitude that with the increase of fracture depth, that is, the diameter of simulated broken wire, the change of leakage magnetic field amplitude also increases gradually. This result is consistent with the simulation results obtained based on the magnetic dipole model. It can be judged that the simulation results are consistent with the theoretical analysis.

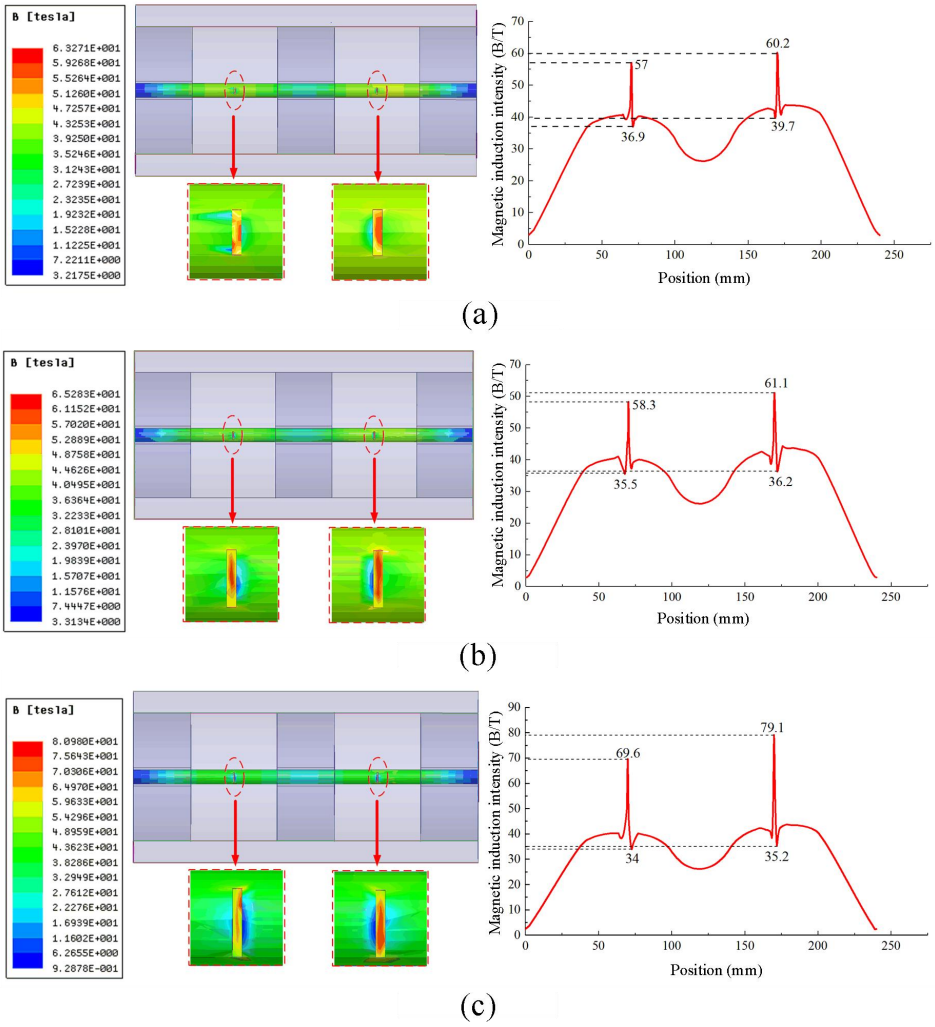

Figure 6 Simulation Results of Leakage Magnetic Field for Wire Rope Damage: (a) Fracture Depth of 0.6 mm, (b) Fracture Depth of 1 mm, (c) Fracture Depth of 1.6 mm

Table 3 Relationship between Fracture Depth and Leakage Magnetic Field Intensity of Damage

Breakage depth (mm)	Peak-to-peak value of the left-side leakage magnetic field (T)	Peak-to-peak value of the right-side leakage magnetic field (T)
0.6	20.1	20.5
1	22.8	24.9
1.6	35.6	43.9

3 SIGNAL EXTRACTION AND RECOGNITION OF WIRE ROPE WEAR

3.1 Suppression of Stock Wave Noise Signals

Due to the repeatability of the wire rope structure, it will show a periodic signal after excitation, but the amplitude is weak. The structure of the wire rope itself leads to the generation of the wave signal, which will interfere with the detection of the damage signal. Therefore, this paper superimposes the two signals with different intensities collected by the two-stage detection module, and superimposes the two intensity signals generated at the same position. The signal can be superimposed by Eqs. (1) , (2) and (3):

$$X_i=\frac{x_i+x_{i+n_0}}{2}\left(i=1,\ 2,\ \ldots\ldots,m\right) \tag{1}$$

$$n_0=\frac{L}{d_0} \tag{2}$$

$$d_0=\frac{\pi D}{N_0} \tag{3}$$

Where i is the pulse sequence number corresponding to the signal, m is the maximum number of pulses, n0 is the offset pulse interval in μs, l is the sensor spacing in μm, d0 is the acquisition distance corresponding to each pulse in μm, d is the diameter of friction wheel in μm, n0 is the number of encoder pulses.

Since the offset superposition method cannot guarantee the complete elimination of the signal spikes generated by the random noise signal, the moving average filtering algorithm is used for further noise reduction processing. The moving average filtering algorithm performs averaging processing within a certain sampling period. In this method, N consecutive values are used as a cyclic queue. The data obtained by each sampling follows the queue ' first in, first out ' principle, and then the average value of N data is calculated, which is used as the sampling value, as shown in Eq. (4):

$$f_n(x)=\frac{x_{n-m+1}+x_{n-m+2}+\ldots+x_{n-1}+x_n}{m} \quad (4)$$

Where fn (x) is the output signal value of the nth sampling period, xn-m + 1, xn-m + 2,..., xn is the signal value in the current sampling period.

Figure 7 is the damage signal waveform diagram under different sampling numbers. It can be seen from the diagram that although there is no obvious wave signal in the original superimposed signal, there are still sharp points. After the sliding average filtering with a sampling number of 5, the signal cusps are effectively removed, and the peak-to-peak value is affected to a certain extent. When the sampling number is 8, the curve is smoother when the relative sampling number is 5, but the peak-to-peak value is affected by the filtering algorithm, which is reduced to a certain extent. When the sampling number is 12, the smoothness of the curve is not much different from that when the sampling number is 8, but the peak-to-peak value changes significantly and the weakening degree is large. If the damage degree is light and the peak-to-peak value of the damage signal is low, the damage signal may be removed by the filtering algorithm, which affects the damage identification. Therefore, the sliding average filtering method with a sampling number of 5 is used to further reduce the noise of the damage signal after offset superposition.

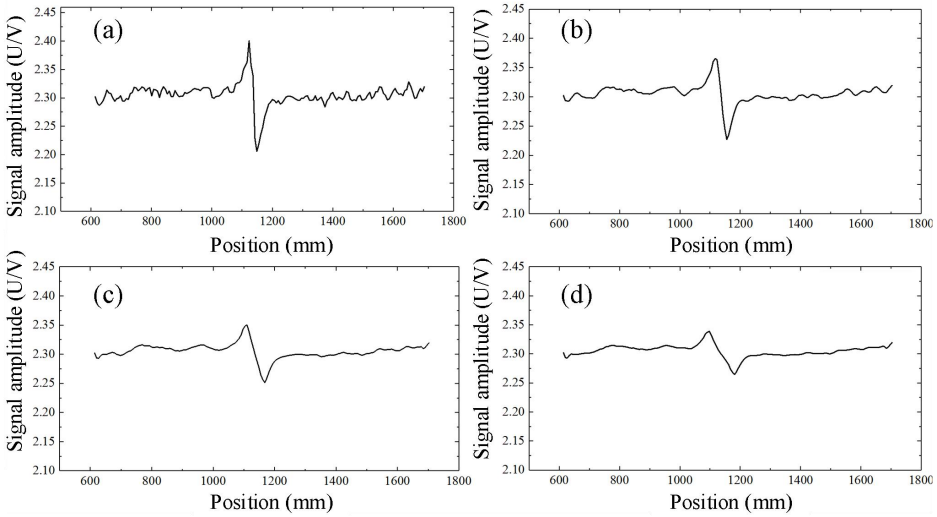

Figure 7 Noise Reduction Results for Different Sampling Numbers: (a) Superimposed Signal, (b) Sampling Number 5, (c) Sampling Number 8, (d) Sampling Number 12

3.2 Extraction and Calibration of Damage Detection Signals

The typical value of the damage signal is determined by simulating the broken wire damage and measuring its signal. The intact wire rope is taken as the basic part of the test, and the defects with a depth of 0.6 mm, 1.2 mm, 1.8 mm, 3 mm, 6 mm and a width of 1 mm are processed by EDM etching in the middle of the wire rope section, as shown in Figure 8. It contains 3, 6, 13, 24, 36 external broken wires respectively.

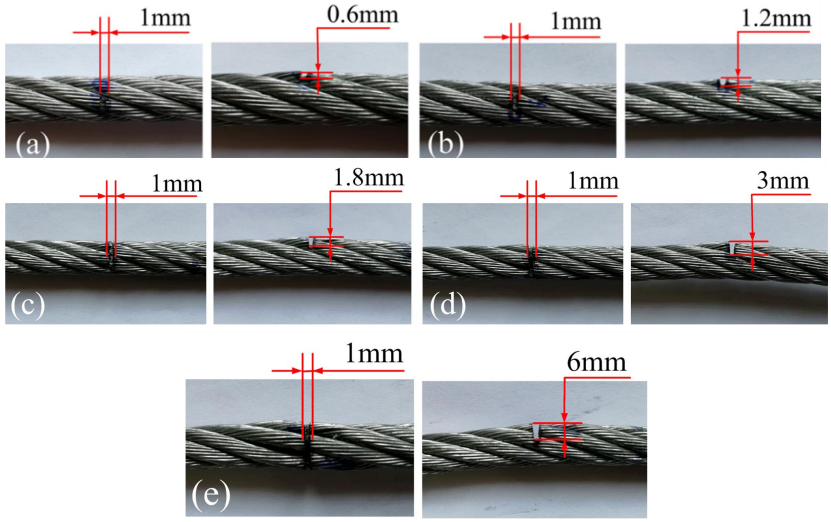

Figure 8 Sample of Steel Wire Rope Damage: (a) 3 Broken Wires, (b) 6 Broken Wires, (c) 13 Broken Wires, (d) 24 Broken Wires, (e) 36 Broken Wires

The wire rope damage sample and the intact wire rope are respectively extracted by the detection device, and the result surface diagram and contour map are extracted, as shown in Figure 9. It can be seen from Figure 9 (a) that the leakage magnetic field of the intact wire rope is evenly distributed, and the signal intensity difference is small. Due to the structure of the wire rope itself, the signal image shows a certain regularity, but the expression of the strand wave signal is not obvious after suppression. Figure 9 (b) corresponds to the wire rope damage is shallow, the number of broken wire is less, the damage signal is not obvious in the figure, but by determining the maximum value of the damage signal, the size and location of the damage signal can be determined. It can be seen from the figure that the damage occurs near the No.6 sensor, the damage of the wire rope corresponding to Figure 9 (c) occurs below the No.5 sensor. Due to the deepening of the damage depth of the wire rope, the intensity of the magnetic flux leakage field is improved, and the circumferential range extends to the No.4 and No.6 sensors. In Figure 9 (d), the damage depth is deepened, the number of broken wires is increased to 24, and the peak and trough of the signal are obvious, which mainly occurs under No.4 and No.5 sensors. At the same time, the leakage magnetic field extends to the bottom of No.1, No.2, No.3 and No.6 sensors, that is, the leakage magnetic field is affected around the damage. In Figure 9 (e), the damage depth is 3 mm, and the damage width is almost the same as the diameter of the wire rope. Therefore, the damage signal is shown in the area below the No.4, No.5 and No.6 sensors, and the No.1, No.2 and No.3 sensors can collect the leakage magnetic field signal at the same time. The amplitude of the damage signal in Figure 9 (f) is large. It can be clearly seen in the figure that compared with the first four kinds of deep damage, the span of the leakage magnetic field signal increases greatly, and the No.1, No.2 and No.3 sensors collect strong leakage magnetic field signals at the same time. This is because the damage with a depth of 6 mm has exceeded the radius of the wire rope, and a certain leakage magnetic field is generated on the undamaged surface of the wire rope.

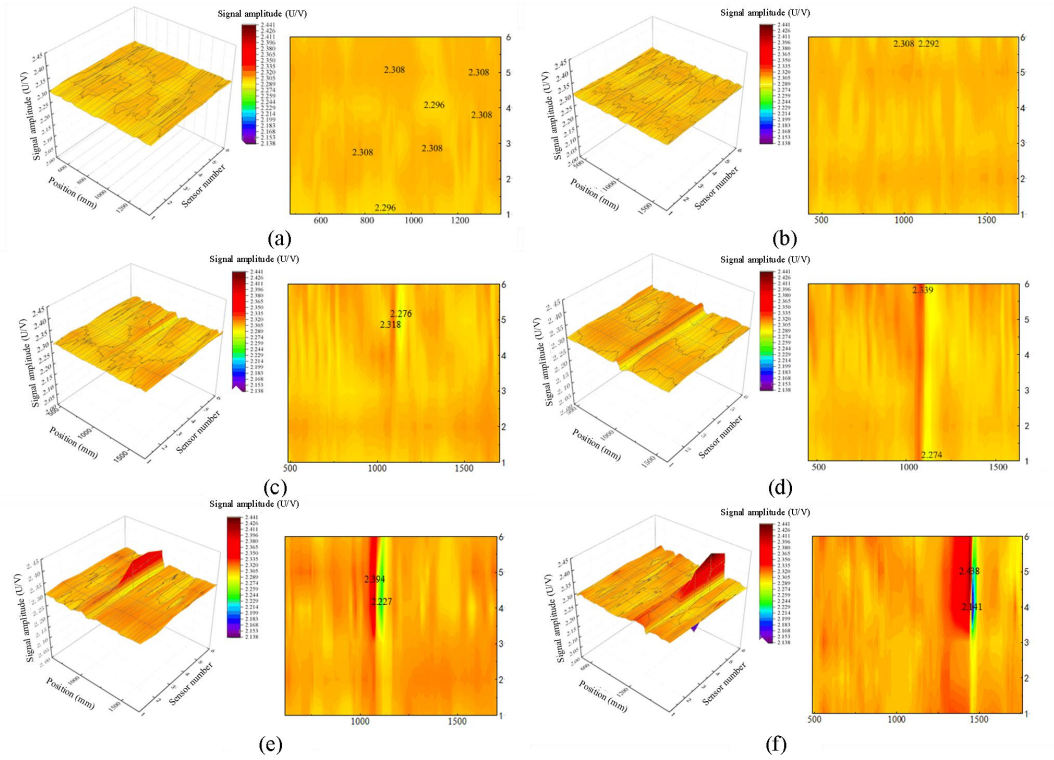

Figure 9 Damage Signal of Standard Sample: (a) Intact Steel Wire Rope, (b) 3 Broken Wires, (c) 6 Broken Wires, (d) 13 Broken Wires, (e) 24 Broken Wires, (f) 36 Broken Wires

3.3 Quantification of Steel Wire Rope Wear Detection Signals

After the peak-to-peak statistics of the damage signal generated by each damage, the results are shown in Table 4.

Table 4 Peak-to-Peak Values of Broken Wire Damage Signals

Number of external broken wires	Peak-to-peak value (V)
0	0.012
3	0.014
6	0.042
13	0.065
24	0.113
36	0.297

Due to the special structure and surface morphology of the wire rope, there is no linear relationship between the peak-to-peak value of the damage signal and the number of broken wires. Therefore, the peak-to-peak value of the obtained damage signal and the number of external broken wires are fitted by second-order polynomial and third-order polynomial respectively. The original change curve and the fitting curve are shown in Figure 10.

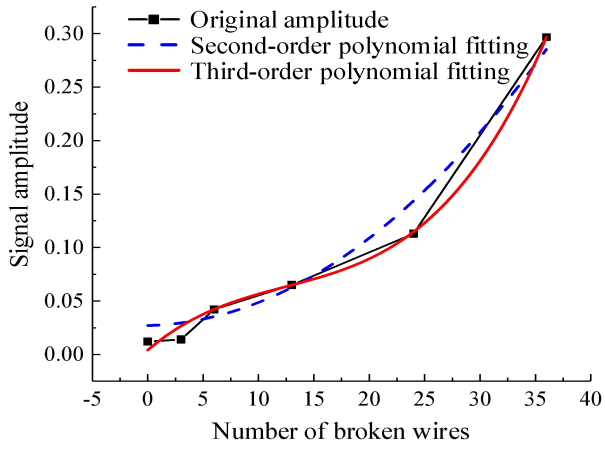

Figure 10 Curve Showing the Peak-to-Peak Value of the Damage Signal Varying with the Number of External Broken Wires

The function relationship between the number of external broken wires and the peak-to-peak variation of the leakage magnetic field signal obtained by fitting with a second-order polynomial is as follows:

$$f_1(x)=0.02711+2.23353\times10^{-4}x+1.9307\times10^{-4}x^2 \quad (5)$$

The coefficient of determination R2 is 0.966.

The function relationship between the number of external broken wires and the peak-to-peak variation of the leakage magnetic field signal obtained by fitting with a third-order polynomial is as follows:

$$f_2(x)=0.00407+0.00883x-4.88021\times10^{-4}x^2+1.30157\times10^{-5}x^3 \quad (6)$$

The coefficient of determination R2 is 0.995.

From the curve changes in Figure 10, it can be seen that the coefficient of determination R2 of the second-order polynomial fitting function is 0.966, which is lower than the coefficient of determination 0.995 of the third-order polynomial fitting result. The function curve obtained by the third-order polynomial fitting is monotonically increasing, and the slope of the curve decreases first and then increases with the number of broken wires, which is consistent with the conclusion obtained from the test results. Therefore, Eq. (6) is used as a quantitative identification function.

4 WIRE ROPE FRACTURE AND BROKEN WIRE TEST

4.1 Design of Magnetic Field Leakage Test for Wire Rope Wear Detection

Using the self-made wire rope sliding friction and wear tester, different degrees of damage were generated on the surface of 7 wire ropes, and the damage morphology is shown in Figure 11. Through observation, it is found that the number of broken wires of these seven worn wire ropes is 5, 3, 5, 6, 6, 5, respectively.

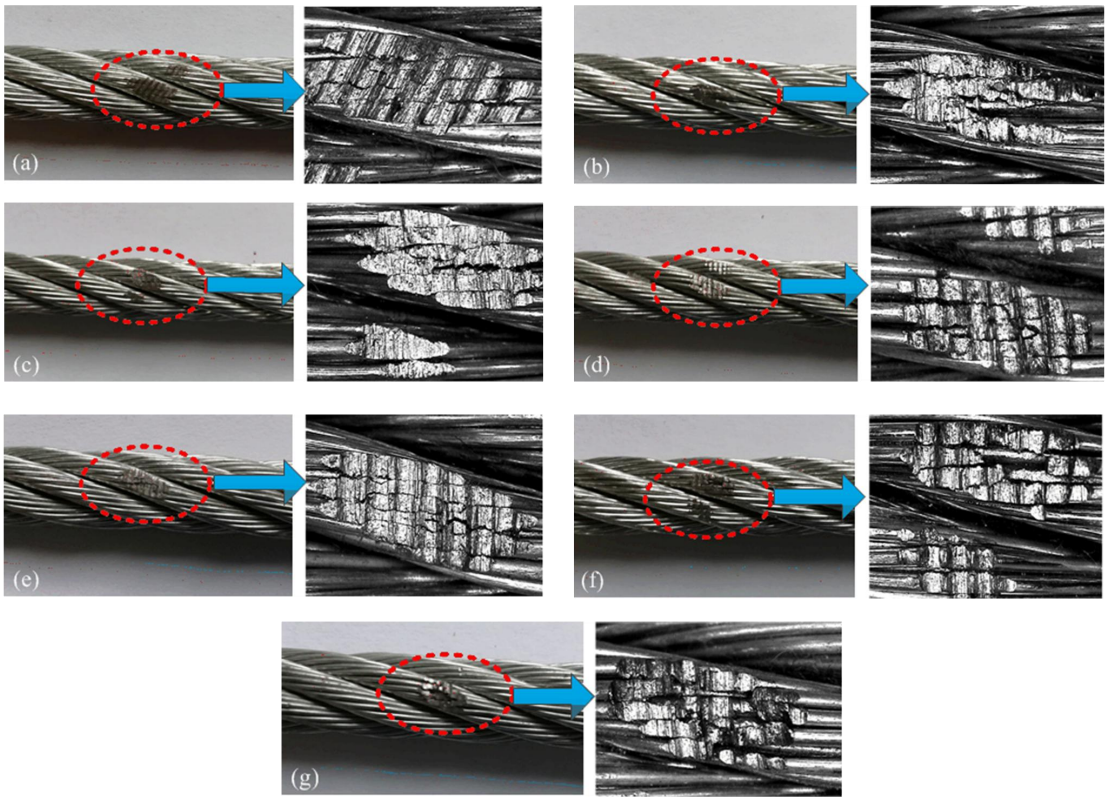

Figure 11 Damage Detection Sample: (a) Sample 1 has 5 Broken Wires, (b) Sample 2 has 3 Broken Wires, (c) Sample 3 has 5 Broken Wires, (d) Sample 4 has no Broken Wire, (e) Sample 5 has 1 Broken Wire, (f) Sample 6 has 1 Broken Wire, (g) Sample 7 has 5 Broken Wires

The test mainly detects the wear and broken wire damage caused by friction and wear on the surface of the wire rope. Firstly, the damage signal of the prepared wire rope sample is extracted by using the designed wire rope nondestructive testing device (as shown in Figure 12). Secondly, according to the signal processing method, the damage signal is processed by offset superposition and noise reduction. Then, the width of the wear scar is judged according to the obtained signal, and the number of broken wire damage is judged by the fitting function relationship. Finally, the damage detection results obtained from the test are compared with the actual observation values to determine the accuracy of damage signal identification and functional relationship.

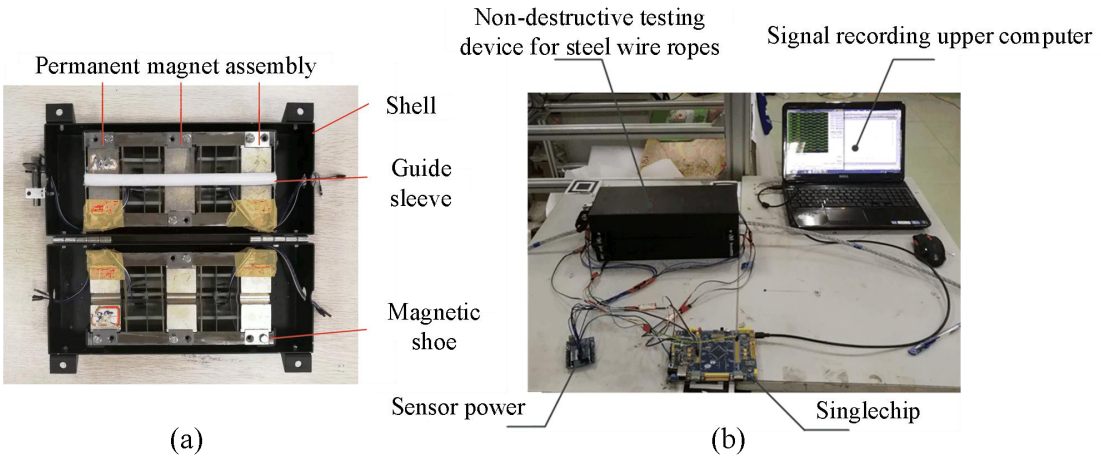

Figure 12 Non-Destructive Testing System for Steel Wire Ropes: (a) Non-Destructive Testing Device for Steel Wire Ropes, (b) Non-Destructive Testing System for Steel Wire Ropes

4.2 Design of Magnetic Field Leakage Test for Wire Rope Wear Detection

Based on the above test device and sample, the signal acquisition and processing of 7 damaged wire rope samples are carried out to obtain the peak-to-peak value of the damage signal, and the damage signal surface diagram of 7 groups of samples is shown in Figure 13. Figure 13 (a) - (g) corresponds to the damaged sample a-g in turn. It can be seen from the diagram that there will be obvious signal intensity changes at the place where the damage occurs, and the degree of damage determines the degree of damage signal intensity change. In addition, the change trend of the signal can be intuitively seen by the degree of surface fluctuation in the surface map. In addition, the leakage magnetic field signal of the worn steel wire rope has a certain degree of periodic fluctuation. The surface diagram is expressed as a wavy surface, but the period is less than the wave signal. The analysis shows that the reason for this phenomenon is: in the friction and wear testing machine, it is necessary to apply pre-tightening force to the wire rope to maintain the tension and bending state. After the test, the wire rope is removed from the test machine. At this time, the wire rope is restored from the tight bending state to the relaxed state. At this time, the pre-tightening force disappears, resulting in a certain degree of rebound of the wire rope, resulting in strand relaxation and wire-to-wire spacing.

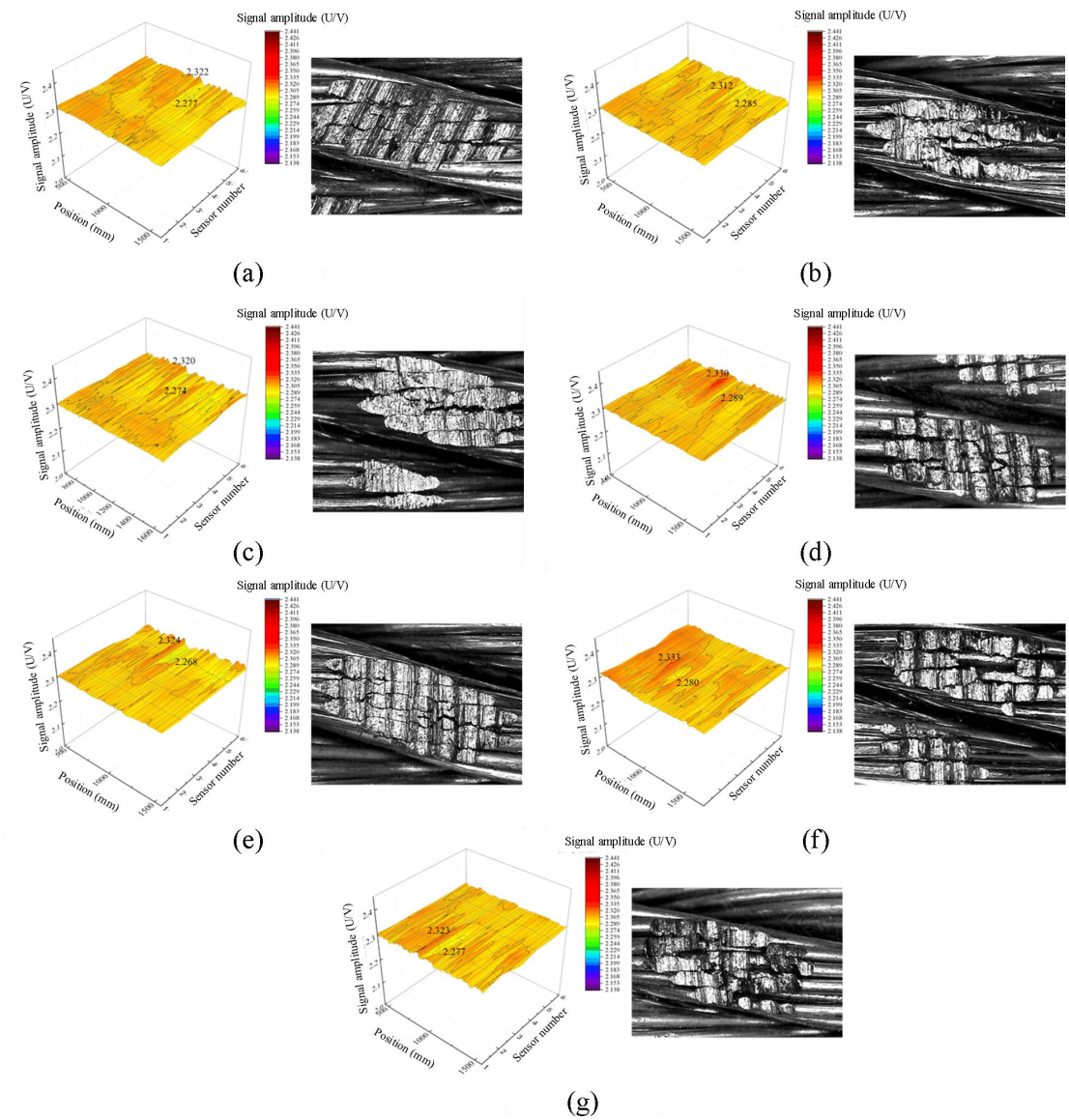

Figure 13 Results of Non-Destructive Testing on Test Specimens: (a) Specimen 1, (b) Specimen 2, (c) Specimen 3, (d) Specimen 4, (e) Specimen 5, (f) Specimen 6, (g) Specimen 7

The statistical results obtained by extracting the peak-to-peak value of the damage signal are shown in Table 5. It can be seen from the table that the size of the peak-to-peak value is directly related to the number of broken wires, but the peak-to-peak values measured between the same number of broken wires are not exactly the same. The main reason is that during the preparation of the sample, after the friction and wear test, although there are broken wires, at the same time, different degrees of wear damage occur around the broken wires. There are differences in the length, width and depth of the wear marks, so there are some differences in the peak-to-peak value of the leakage magnetic field signal. Moreover, it can be found that there is a certain deviation between the number of broken wires obtained by fitting and the actual number of broken wires. The main reason for the deviation is that friction and wear and broken wire damage will produce leakage magnetic field at the same time, and the sample is prepared by friction and wear testing machine. The friction and wear and broken wire damage are concentrated in the same position. The leakage magnetic field signals generated by the two kinds of damage are superimposed on each other, so that the number of broken wires obtained by fitting the measured peak-to-peak signal is higher than the actual number of broken wires. In addition, since the fitting function relationship is obtained by numerical calculation and fitting of the test data, the function fitting method itself has a certain error, which is determined by the method itself and the data sample size, so there is a certain deviation in the judgment of the number of broken wires. On the other hand, the error of the measurement results is caused by the leakage magnetic field caused by the wear damage except the broken wire. It can be seen from the results that the more the number of broken wires, the greater the error of the results, which indicates that the degree of wear damage is more serious, which is consistent with the results of observing the damage morphology.

Table 5 Test Results of Damaged Samples

Number	Actual number of broken wires	Peak-to-peak value (V)	Detection value	Error

1	5	0.045	6.32	26.4%
2	3	0.027	3.08	2.7%
3	5	0.046	6.43	28.6%
4	6	0.049	6.77	12.8%
5	6	0.056	7.65	27.5%
6	6	0.056	7.65	27.5%
7	5	0.046	6.43	28.6%

In order to further explain the damage detection performance of the non-destructive testing device, the detection device and method of this paper are compared with the existing non-destructive testing device. Two wire ropes of the same specifications were selected. Before the start of the test, two damages were artificially manufactured on the surface of the wire rope (see Figure 14). Among them, the No.1 damage was three broken wires at a position of 9 m, the No.2 damage was 11 broken wires and severe wear, located at 10.5 m.

Figure 14 Damage Morphology of the Sample

Figure 15 shows the test results of the two detection devices. It can be seen from Figure 15 (a) that a total of four damages were detected by this type of non-destructive detector. Among them, damage 3 at 10.5 m corresponded to No.2 damage in Table 6. However, the detected damage amount was only 0.57 %, and the diameter shrinkage equivalent was only 0.03 mm, which was quite different from the actual damage situation. And three broken wires at No.1 damage were not detected. In the other three damage locations, no obvious rust damage was found after manual inspection. The non-destructive testing device for wire rope developed in this paper is more accurate in identifying the damage of wire rope No.1 (3 broken wires). Due to the bending deformation at one end of the broken wire, the fracture shape is irregular, and the distribution of the leakage magnetic field signal is complex, so the axial fluctuation area of the damage signal wire rope is large. The wear damage of No.2 is identified as 12.1 broken wires, and the number of broken wires is more than the actual number of broken wires. This is because the wear damage is serious and the wear area is large, which leads to the high detection result. Due to the large wear range of No.2 damage along the axial direction of the wire rope, the figure shows that there is a high signal amplitude area before the peak value of the damage signal.

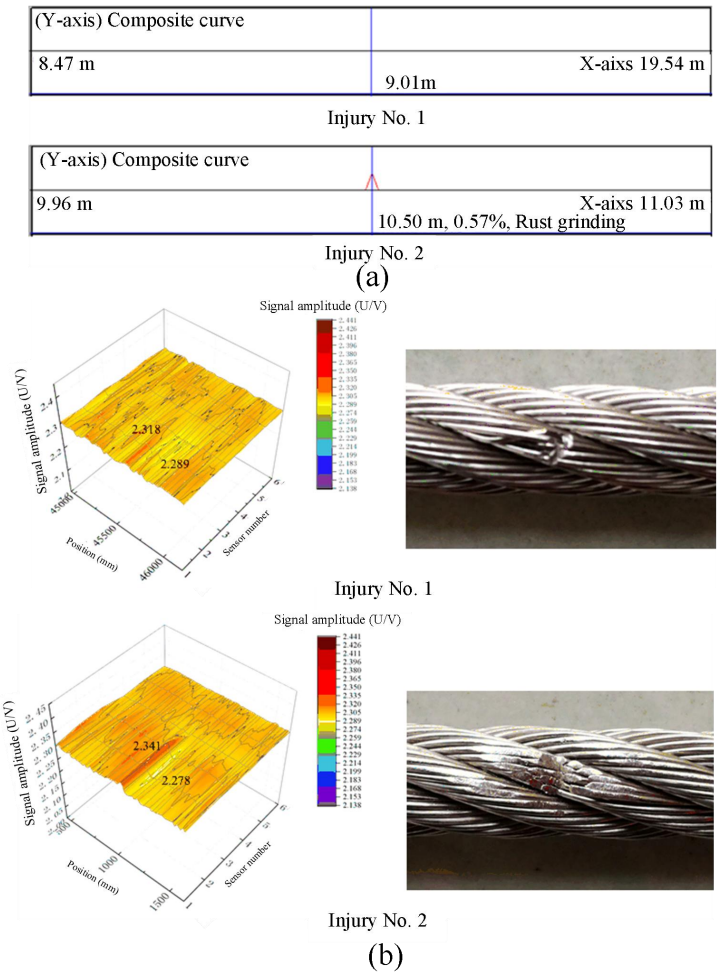

Figure 15 Comparison of Results of Non-Destructive Testing Devices for Steel Wire Ropes: (a) Non-Destructive Testing Product for Steel Wire Ropes, (b) The Device Developed in this Paper

Through the above comparative tests, it can be seen (Table 6) that the existing non-destructive testing instrument of this type of wire rope still has a low accuracy in the quantitative detection results of wire rope damage, and there are certain errors and missed detection and wrong detection. The error rate is as high as 51.3 %. The non-destructive testing device and method studied in this paper have high accuracy in the detection of wire rope wear damage and broken wire, and the error is reduced to 13.3 %.

Table 6 Statistical Results of Damaged Steel Wire Rope Detection

Number	Type of injury	Degree of injury	Detection result	Error
1	Fracture of wire	3 broken wires	3.4 broken wires	13.3%
2	Wear, broken wires	1.2 mm, 8 broken wires	12.1 broken wires	51.3%

5 CONCLUSIONS

This paper presents a dual-stage excitation structure employing asymmetric magnetic poles and differentiated grades of NdFeB magnets, coupled with a corresponding signal processing method, aiming to achieve and enhance the accuracy of non-destructive testing for wear and broken wire damage in steel wire ropes. The main conclusions are as follows:

1. The innovative design and optimization of the dual-stage excitation structure significantly improve the magnetic excitation effect and damage identification capability. By adopting an asymmetric magnetic pole arrangement composed of left, middle, and right pole sets with a specific grade combination (N35/N52/N52), combined with a 60 mm pole spacing, two independent excitation intervals with a significant difference in magnetic excitation intensity (up to 7.7%) are formed within the steel wire rope.
2. The grade of the permanent magnets and the magnetic pole spacing are key factors affecting the distribution and difference in magnetic excitation intensity. Using N35 grade magnets with a 60 mm spacing results in the largest intensity difference between the left and right excitation intervals. Simultaneously, the generated demagnetization zone helps form two independent excitation environments for damage, thereby optimizing the contrast of leakage magnetic field signals.
3. The signal processing method based on offset superposition and sliding average filtering effectively suppresses strand wave noise interference. By superimposing the two intensity signals collected by the dual-stage detection module, the

periodic strand wave noise and random spikes inherent to the wire rope's structure are significantly eliminated, enhancing the signal-to-noise ratio and identifiability of the damage signals.

4.By preparing and testing steel wire rope samples with varying damage degrees, a third-order polynomial quantitative relationship between the number of broken wires and the peak-to-peak value of the leakage magnetic field signal was established (coefficient of determination $R^2 = 0.995$). Compared to an existing testing device, the method proposed in this paper reduces the error rate in broken wire identification from 51.3% to 13.3%, significantly improving the accuracy and reliability of damage identification, especially demonstrating superior performance in detecting combined wear and broken wire damage.

COMPETING INTERESTS

The authors have no relevant financial or non-financial interests to disclose.

FUNDING

This research was funded by the Key Laboratory of Intelligent Operation and Maintenance of High-parameter Lifts, State Administration for Market Regulation (JSTJ-IOMHL-202505). This project is also supported by the National Natural Science Foundation of China (Grant No. 52475234).

REFERENCES

[1] George AC. Theory of Wire Rope, 2rd ed. Springer Science & Business Media: Berlin, Germany, 2012: 1-29.
[2] Laguerre L, Aime JC, Brissaud M. Magnetostrictive pulse-echo device for non-destructive evaluation of cylindrical steel materials using longitudinal guided waves. Ultrasonics, 2002, 39(7): 503-514.
[3] Cruzado A, Urchegui MA, Gómeza X. Finite element modelling and experimental validation of fretting wear scars in thin steel wires. Wear, 2012, 289: 26-38.
[4] Cruzado A, Urchegui MA, Gómeza X. Finite element modelling of fretting wear scars in the thin steel wires: Application in crossed cylinder arrangements. Wear, 2014, 318(1): 98-105.
[5] Cruzado A, Leen SB, Urchegui MA, et al. Finite element simulation of fretting wear and fatigue in thin steel wires. International Journal of Fatigue, 2013, 55: 7-21.
[6] Wang DG, Zhang DK, Ge SR. Effect of terminal mass on fretting and fatigue parameters of a hoisting rope during a lifting cycle in coal mine. Engineering Failure Analysis, 2014, 36: 407-422.
[7] Wang DG, Zhang DK, Ge SR. Finite element analysis of fretting fatigue behaviour of steel wires and crack initiation characteristics. Engineering Failure Analysis, 2013, 28: 47-62.
[8] Wang DG, Zhang DK, Ge SR. Fretting-fatigue behaviour of steel wires in low cycle fatigue. Materials & Design, 2011, 32(10): 4986-4993.
[9] Liu YH, Luo WS, Mao LC, et al. Wear fatigue fracture characteristics of different steel wire ropes and mechanism analysis. Mechanics Based Design of Structures and Machines, 2025.
[10] Chang XD, Peng YX, Zhu ZC, et al. Evolution properties of tribological parameters for steel wire rope under sliding contact conditions. Metals, 2018, 8(10): 1-16.
[11] Peng YX, Chang XD, Zhu ZC, et al. Sliding friction and wear behaviour of winding hoisting rope in ultra-deep coal mine under different conditions. Wear, 2016, 368: 423-434.
[12] Wang B, Wang DG, Ye JH, et al. Effect of fatigue load on the bending tribo-corrosion-fatigue behaviors between the main cable wires. Friction, 2024, 12: 1512-1531.
[13] Mazurek P, Roskosz M. Influence of the Earth's magnetic field on the diagnosis of steel wire rope by passive magnetic methods. Journal of Magnetism and Magnetic Materials, 2022, 547: 168802.
[14] Zhang DL, Zhang EC, Yan XL. Quantitative method for detecting internal and surface defects in wire rope. NDT & E International, 2021, 119: 102405.
[15] Yan XL, Zhang DL, Zhao F. Improve the signal to noise ratio and installation convenience of the inductive coil for wire rope nondestructive testing. NDT & E International, 2017, 92: 221-227.
[16] Yan XL, Zhang DL, Pan SM, et al. Online nondestructive testing for fine steel wire rope in electromagnetic interference environment. NDT & E International, 2017, 92: 75-81.
[17] Liu SW, Sun YH, Jiang XY, et al. Comparison and analysis of multiple signal processing methods in steel wire rope defect detection by hall sensor. Measurement, 2021, 171: 108768.
[18] Zhang DL, Zhang EC, Pan SM. A new signal processing method for the nondestructive testing of a steel wire rope using a small device. NDT & E International, 2020, 114: 102299.
[19] Zheng PB, Zhang JW. Quantitative nondestructive testing of wire rope based on pseudo-color image enhancement technology. Nondestructive Testing and Evaluation, 2019, 34(3): 221-242.
[20] Li X, Zhang JW, Shi JZ. Quantitative nondestructive testing of broken wires for wire rope based on magnetic and infrared information. Journal of Sensor and Sensor Systems, 2020, 3: 1-14.
[21] Liu SW, Sun YH, Jiang XY, et al. A new MFL imaging and quantitative nondestructive evaluation method in wire rope defect detection. Mechanical Systems and Signal Processing, 2022, 163: 108156.
[22] Li JG, Zhang JW. Quantitative nondestructive testing of wire rope using image super-resolution method and adaBoost classifier. Shock and Vibration, 2019, 4: 1-13.

[23] Cao QS, Liu D, He YH, et al. Nondestructive and quantitative evaluation of wire rope based on radial basis function neural network using eddy current inspection. NDT & E International, 2012, 46: 7-13.
[24] Peng Y, Liu J, He J, et al. Steel wire rope damage width identification method based on residual networks and multi-channel feature fusion. Machines, 2024, 12(11): 744.
[25] Paweł M, Maciej R, Jerzy K. Analysis of the resolution of the passive magnetic method on the example of nondestructive testing of steel wire ropes. Journal of Magnetism and Magnetic Materials, 2024, 589: 171607.
[26] Lu SL, Zhang JW. Quantitative nondestructive testing of wire ropes based on features fusion of magnetic image and infrared image. Shock and Vibration, 2019, 2019: 1-15.
[27] Feng JP, Li JL, Gao K, et al. Portable automatic detection system with infrared imaging for measuring steel wires corrosion damage. Automation in Construction, 2023, 156: 105080.
[28] Neslušan M, Bahleda F, Minárik P, et al. Non-destructive monitoring of corrosion extent in steel rope wires via Barkhausen noise emission. Journal of Magnetism and Magnetic Materials, 2019, 484: 179-187.
[29] Zhang GY, Tang ZH, Zhang J, et al. Convolutional autoencoder-based flaw detection for steel wire ropes. Sensors, 2020, 20(22): 6612.
[30] Larsson J, Jansson A, Pejryd L. Process monitoring of the wire drawing process using a web camera based vision system. Journal of Materials Processing Technology, 2017, 249: 512-521.
[31] Zhou P, Zhou GB, He ZZ, et al. A novel texture-based damage detection method for wire ropes. Measurement, 2019, 148: 1-14.
[32] Chen Q, Zhang J, Ye Q. Wire rope damage detection based on magnetic leakage and visible light. Journal of Failure Analysis and Prevention, 2023, 23(3): 1275-1287.
[33] Huang X, Liu Z, Zhang X, et al. Surface damage detection for steel wire ropes using deep learning and computer vision techniques. Measurement, 2020, 161: 107849.
[34] Zhou P, Zhou GB, Wang HL, et al. Automatic detection of industrial wire rope surface damage using deep learning-based visual perception technology. IEEE Transactions on Instrumentation and Measurement, 2021, 70: 5002911.